

# InP-based waveguide photodiodes heterogeneously integrated on silicon-on-insulator for photonic microwave generation

Andreas Beling,<sup>1,\*</sup> Allen S. Cross,<sup>1</sup> Molly Piels,<sup>2</sup> Jon Peters,<sup>2</sup> Qiugui Zhou,<sup>1</sup> John E. Bowers,<sup>2</sup> and Joe C. Campbell<sup>1</sup>

<sup>1</sup>ECE Department, University of Virginia, 351 McCormick Road, Charlottesville, VA 22904, USA

<sup>2</sup>ECE Department, University of California, Santa Barbara, CA 93106, USA

\*andreas@virginia.edu

**Abstract:** High-linearity modified uni-traveling carrier photodiodes on silicon-on-insulator with low AM-to-PM conversion factor are demonstrated. The devices deliver more than 2.5 dBm RF output power up to 40 GHz and have an output third order intercept point of 30 dBm at 20 GHz. Photodiode arrays exceed a saturation current-bandwidth-product of 630 mA·GHz and reach unsaturated RF output power levels of 10 dBm at 20 GHz.

©2013 Optical Society of America

**OCIS codes:** (230.5170) Photodiodes; (040.5160) Photodetectors; (060.5625) Radio frequency photonics.

---

## References and links

1. D. Liang, G. Roelkens, R. Baets, and J. E. Bowers, "Hybrid integrated platforms for silicon photonics," *Materials* **3**(3), 1782–1802 (2010).
2. H. Park, M. N. Sysak, H.-W. Chen, A. W. Fang, D. Liang, L. Liao, B. R. Koch, J. Bovington, Y. Tang, K. Wong, M. Jacob-Mitos, R. Jones, and J. E. Bowers, "Device and Integration Technology for Silicon Photonic Transmitters," *IEEE J. Sel. Top. Quantum Electron.* **17**(3), 671–688 (2011).
3. H. Park, A. W. Fang, R. Jones, O. Cohen, O. Raday, M. N. Sysak, M. J. Paniccia, and J. E. Bowers, "A hybrid AlGaInAs-silicon evanescent waveguide photodetector," *Opt. Express* **15**(10), 6044–6052 (2007).
4. G. Fish, "Heterogeneous photonic integration for microwave photonic applications," in *Tech. Digest Optical Fiber Commun. OFC 2013* (Optical Society of America, 2013), paper OW3D.5.
5. H. Pan, Z. Li, A. Beling, and J. C. Campbell, "Measurement and modeling of high-linearity modified uni-traveling carrier photodiode with highly-doped absorber," *Opt. Express* **17**(22), 20221–20226 (2009).
6. H. Pan, Y. Fu, Z. Li, and J. C. Campbell, "High-linearity modified uni-traveling carrier photodiodes," in *Tech. Digest Optical Fiber Commun. OFC 2010* (Optical Society of America, 2010), paper OWN1.
7. A. Beling, A. S. Cross, M. Piels, J. Peters, Y. Fu, Q. Zhou, J. E. Bowers, and J. C. Campbell, "High-power high-speed waveguide photodiodes and photodiode arrays heterogeneously integrated on silicon-on-insulator," in *Tech. Digest Optical Fiber Commun. OFC 2013* (Optical Society of America, 2013), paper OM2J.
8. J.-P. Weber, "Optimization of the carrier-induced effective index change in InGaAsP waveguides – applications to tunable bragg filters," *IEEE J. Quantum Electron.* **30**(8), 1801–1816 (1994).
9. B. R. Bennett, R. A. Soref, and J. A. del Alamo, "Carrier-induced change in refractive index of InP, GaAs, and InGaAsP," *IEEE Journal of Quant. Electronics* **26**(1), 113–122 (1990).
10. A. Beling, Y. Fu, Z. Li, H. Pan, Q. Zhou, A. Cross, M. Piels, J. Peters, J. E. Bowers, and J. C. Campbell, "Modified Uni-Traveling Carrier Photodiodes Heterogeneously Integrated on Silicon-on-Insulator (SOI)," in *Conference on Integrated Photonics Research and Silicon Nanophotonics IPR 2012* (Optical Society of America, 2012), paper IM2A.2.
11. M. Piels, A. Ramaswamy, and J. E. Bowers, "Nonlinear modeling of waveguide photodetectors," *Opt. Express* **21**(13), 15634–15644 (2013).
12. T. M. Fortier, F. Quinlan, A. Hati, C. Nelson, J. A. Taylor, Y. Fu, J. C. Campbell, and S. A. Diddams, "Photonic microwave generation with high-power photodiodes," *Opt. Lett.* **38**(10), 1712–1714 (2013).
13. Data sheet XPDV2020, [www.u2t.de](http://www.u2t.de).
14. J. Taylor, S. Datta, A. Hati, C. Nelson, F. Quinlan, A. Joshi, and S. Diddams, "Characterization of power-to-phase conversion in high-speed P-I-N photodiodes," *IEEE Photonics Journal* **3**(1), 140–151 (2011).

## 1. Introduction

Heterogeneous integration of III-V material on a silicon photonics platform through wafer bonding has been demonstrated as a technique to integrate dissimilar materials without compromising their own properties [1]. While this approach is particularly interesting for silicon transmitters [2], it also leads to low dark current photodiodes with high efficiencies beyond 1.55  $\mu\text{m}$  [3]. Furthermore, heterogeneous integration has the potential to fully exploit bandgap engineering available in III-V materials to design more complex detector heterostructures.

In the present work we use a wafer-bonding technology [1] to integrate high-power high-linearity III-V photodiodes on silicon-on-insulator (SOI) waveguides. We report on the design and experimental results including bandwidth, saturation current, output third order intercept point (IP3), and AM-to-PM conversion factor. Based on the experimental results we believe that our devices are well suited for the use in heterogeneous silicon based photonic integrated circuits for microwave photonic applications [4].

## 2. Design and fabrication

The III-V on SOI layer structure is shown in Fig. 1. It is based on a previously demonstrated normal-incidence InGaAsP/InP modified uni-traveling carrier (MUTC) photodiode (PD) that has achieved high saturation current and high linearity [5]. The InGaAs absorbing region is comprised of a 250 nm p + and a 50 nm not-intentionally-doped (n.i.d.) absorber layer. In order to form an abrupt doping profile, Be is used as the dopant in the p + absorbing layer. The highly p-doped undepleted InGaAs absorber has been shown to significantly reduce the voltage dependent capacitance contribution to intermodulation distortion at higher frequencies [6]. A 700 nm n.i.d. InP drift layer is inserted between the absorber and the n + contact layer to reduce junction capacitance. Thin bandgap-graded InGaAsP layers are used to smooth the

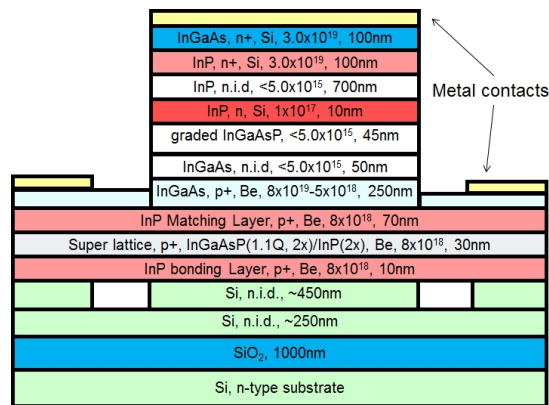


Fig. 1. Layer stack design of MUTC PD on SOI. Doping concentrations in  $\text{cm}^{-3}$ .

abrupt band barrier at the InGaAs–InP heterojunction interface. The structure also incorporates a 10 nm moderately n-type doped InP cliff layer to maintain high electric field at the absorber-drift layer interface. This is crucial to achieving high saturation current. A 10 nm thick bonding layer and an InP/InGaAsP super lattice are integrated below the p + contact layer to facilitate wafer bonding onto Si and to reduce the propagation of defects into the active region. The PD is evanescently coupled to an underlying SOI waveguide. The thickness of the Si rib and buried oxide layer are 0.7  $\mu\text{m}$  and 1  $\mu\text{m}$ , respectively. The fabrication process starts with dry etching of the SOI waveguides. The passive input waveguide is 2  $\mu\text{m}$  wide and is tapered to 14(10)  $\mu\text{m}$  in order to match the width of the active PD region. We chose a relatively large PD width to reduce the optical peak intensity in the

absorber and thus improve saturation current. The III-V structure was transferred to the patterned Si through low-temperature oxygen-plasma-assisted wafer bonding [3]. After removal of the InP substrate, we deposited an AuGe/Ni/Au blanket metallization and used self-aligned inductively coupled plasma reactive ion etching (ICP-RIE) to form the n-mesa. Next, the p-mesa was etched, the p-contact metal layers were evaporated, and devices were passivated with a 200 nm-thick SiO<sub>2</sub> film. The probe pads were deposited on a 2.5 μm-thick SU8 layer to reduce RF loss originating from the low resistivity Si substrate [7].

### 3. Experimental results

Waveguide (WG) MUTC PDs with mesa lengths of 100 μm, 50 μm, and 25 μm were fabricated. We measured typical dark currents below 10 nA at 5 V reverse bias voltage. Using a lensed fiber with a spot diameter of approximately 2 μm we measured responsivities of 100 μm-long PDs up to 0.26 A/W at 1.55 μm wavelength (no anti-reflection coating). For 50 μm and 25 μm PDs we obtained 0.25 A/W and 0.11 A/W which suggests that most of the light absorption occurs within the first 50 μm. Based on this result and taking the simulated fiber-chip coupling and reflection losses of 5.1 dB into account, we estimated the internal responsivities to be as high as 0.85 A/W.

To measure the bandwidth, we used an optical heterodyne setup with an optical modulation depth close to 100%. PDs with lengths of 100 μm, 50 μm, and 25 μm achieved 3dB bandwidths of 15 GHz, 24 GHz and 30 GHz, respectively, as shown in Fig. 2(a). Figure 2(b) summarizes the results from all devices we measured. A comparison with calculations suggests that devices with active areas >500 μm<sup>2</sup> are mostly RC-limited.

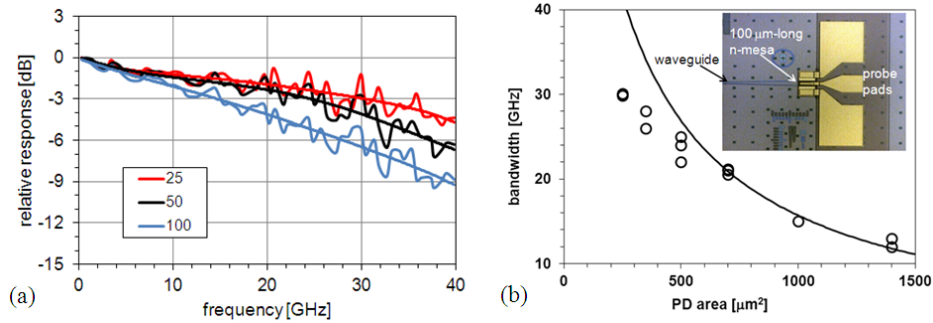


Fig. 2. (a) Calibrated frequency responses of 25 μm, 50 μm, and 100 μm-long waveguide MUTC PDs measured at 5 V bias voltage. (b) Each data point corresponds to a measured device. Line: calculated RC-limited bandwidth using the measured capacitances and series resistances. Inset: Micrograph of fabricated 100-μm long MUTC PD.

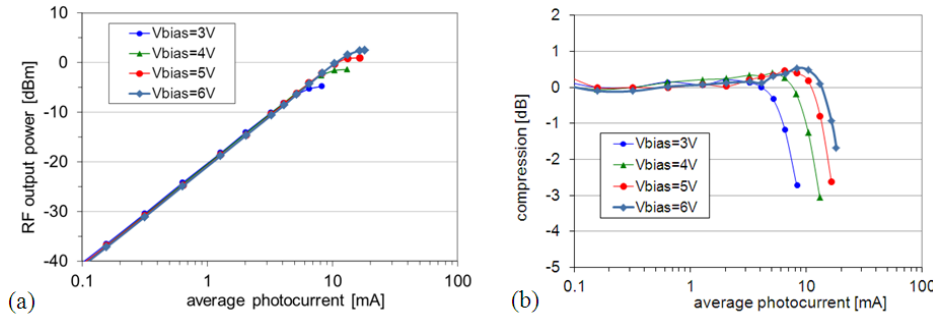


Fig. 3. RF output power (a) and RF compression (b) at 40 GHz.

Maximum RF output power levels and saturation currents (i.e. average photocurrent at 1-dB RF power compression) were measured at room temperature (no temperature control) as a

function of bias voltage. Figure 3 shows results from a 25- $\mu\text{m}$  PD measured at 40 GHz. The RF output power level and saturation current were 2.5 dBm and 17 mA at 6 V, respectively. The highest output power of a 14x100  $\mu\text{m}^2$  PD before thermal failure was 8 dBm at 10 GHz, 8 V, and 25 mA. Table 1 summarizes responsivities, 1-dB saturation currents and RF output power levels of 100  $\mu\text{m}$ , 50  $\mu\text{m}$ , and 25  $\mu\text{m}$  devices, all measured at 6 V and 50  $\Omega$  external load. While the smallest PD has the lowest saturation current we find that going from 50- $\mu\text{m}$  to 100- $\mu\text{m}$  long PDs does not significantly improve saturation current. We attribute this behavior to the non-uniform illumination profile in the absorber and to the fact that strongest absorption occurs at the input side of the PD. The simulation in Fig. 4(a) illustrates the optical intensity distribution in the plane of the absorber layer. We used commercial beam propagation software and took free carrier effects in the highly doped InGaAs absorber into account by calculating the refractive indices using the method described in [8] and [9]. The result shows that the optical intensity peaks on the first 10  $\mu\text{m}$  and remains considerably lower beyond 40  $\mu\text{m}$ . Assuming that the carrier generation is proportional to the optical intensity, a non-uniform photocurrent distribution follows that can lead to localized areas of strong saturation at high optical input powers.

**Table 1. Performance of waveguide MUTC PDs**

PD active area [ $\mu\text{m}^2$ ]	Fiber-coupled responsivity [A/W]	Saturation current [mA]	Saturation current-bandwidth product [mA-GHz]	Max. RF output power [dBm]
14 x 25	0.11	13	390	+ 3.9 at 30 GHz
14 x 50	0.25	20	480	+ 5.6 at 20 GHz
14 x 100	0.26	21	315	+ 6.7 at 10 GHz

This behavior is in contrast to surface-normal illuminated PDs where nearly perfect uniform illumination can be achieved. A comparison of waveguide and back-illuminated PDs fabricated on one of our previous wafers with the same epitaxial layer stack [10] reveals larger saturation current densities for back-illuminated PDs. As shown in Fig. 4(b), shorter waveguide PDs are approaching the current density of the back-illuminated PD by 75%. The latter defines the upper limit for this particular epitaxial layer structure. The extrapolation of the curves in Fig. 4(b) towards shorter PD lengths suggests that highest saturation current densities can be achieved for WG PDs with lengths between 10  $\mu\text{m}$  and 20  $\mu\text{m}$ . It is worth mentioning that for the 100- $\mu\text{m}$  WG PD at high currents ( $> 20$  mA) and voltages ( $> 6$  V) the saturation current only marginally increases with the applied bias voltage; a fact that may be explained by a decrease in carrier velocities due to joule heating [11].

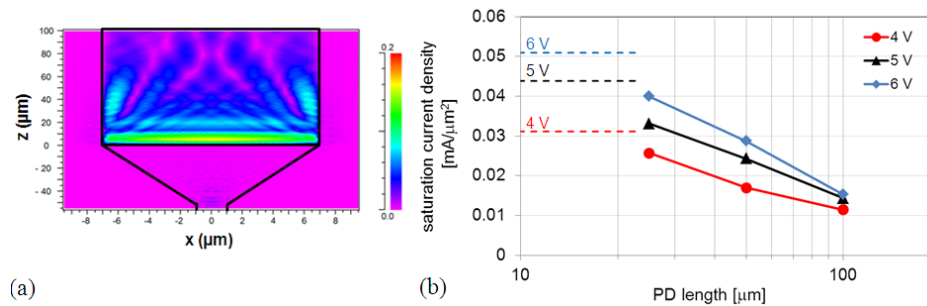


Fig. 4. (a) Relative optical intensity profile in the plane of the absorber. The active PD area extends from  $x = -7$  to  $7$  and  $z = 0$  to  $100$ . The tapered silicon waveguide extends from  $z = 0$  to  $-50$ . (b) Saturation current measured at the 3 dB bandwidth normalized to PD active area as a function of PD length. All WG PDs are 14- $\mu\text{m}$  wide. The dashed lines indicate the upper limits and were measured on a 700- $\mu\text{m}^2$  back-illuminated PD.

It has been shown that high-power, high-linearity photodiodes provide significant advantages in many analog photonic applications including photonic microwave generation [12]. To characterize PD linearity the photocurrent dependence of the output third-order intercept point of a 24-GHz bandwidth PD was measured using a three-tone setup. As shown in Fig. 5(a) the IP3 reaches values as high as 36 dBm at 1 GHz and 30 dBm at 20 GHz; a result that we primarily attribute to the optimized doping profile of our structure [6]. It is worth mentioning that InP-based normal-incidence MUTC PDs in [5] showed very similar IP3 performance in this photocurrent range. A comparison with measured data from a commercial InP waveguide photodiode (bandwidth: 35 GHz, max. rated current: 12 mA at 3.5 V [13]) indicates an improvement in IP3 of up to more than 10 dB.

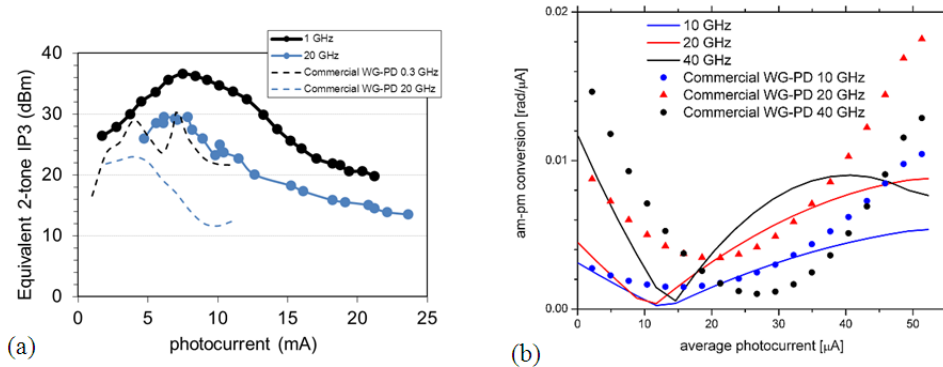


Fig. 5. (a) IP3 vs. average photocurrent. (b) AM-to-PM conversion factor. Solid lines: 14x50  $\mu\text{m}^2$  PD measured at 6 V, symbols: commercial InP WG PD measured at 3 V.

Another limitation in RF signal generation comes from the fact that PD nonlinearities can potentially degrade the spectral purity of the RF signal by coupling amplitude noise on the optical intensity to phase noise on the microwave signal. Thus, a highly-linear PD with small AM-to-PM conversion factor is important to maintain low phase noise [12]. We determined the AM-to-PM conversion factor from pulse response measurements through FFT similar to the method described in [14]. We used a 1.55  $\mu\text{m}$  fs-pulse laser with 100 MHz repetition rate. Figure 5(b) shows the extracted AM-to-PM conversion factor after taking the derivative of the phase with respect to average photocurrent. Very low AM-to-PM conversion was obtained at 10 GHz up to 25  $\mu\text{A}$  (= 0.5 Vpp pulse peak voltage), with zero-crossings also observed at 20 GHz and 40 GHz. We found that our heterogeneously integrated MUTC PD has up to 50% lower AM-PM conversion factor at high photocurrents when compared to the commercial InP-PD.

To further enhance saturation current and RF output power, we designed and fabricated arrays in which the photocurrents of multiple PDs, integrated in parallel, are summed on the output pad. Figures 6(a)-(b) show a 2-PD array in that the optical input signal is coupled into a singlemode waveguide and then equally split in a multi-mode interference (MMI) splitter to feed both PDs. It should be noted that the 10x37  $\mu\text{m}^2$  PDs are located on top of the multi-mode waveguide at positions where optical simulations predicted two-fold self-images. The responsivity excluding coupling loss was 0.2 A/W. The bandwidth for our 2-PD array is 15 GHz, and taking the 42 mA saturation current measured at 20 GHz and 5 V bias, we achieved a record high saturation current-bandwidth-product of greater than 630 mA·GHz for Si integrated PDs. The maximum RF output power reached 9.3 dBm at 20 GHz.

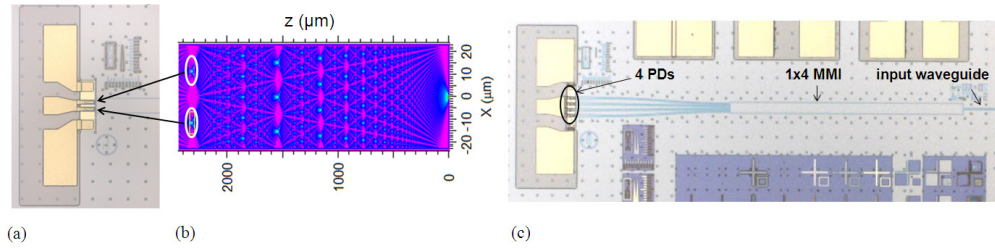


Fig. 6. 2-element PD array: PDs with RF pads (a), simulated intensity distribution in multi-mode waveguide (b) with PD locations being circled. (c) 4-element PD array.

Figure 6(c) shows the 4-element PD array. In this design the input signal is split in a 1x4 MMI splitter ( $40 \times 900 \mu\text{m}^2$ ) to four waveguides, each terminated by a  $10 \times 20 \mu\text{m}^2$  PD. Although this device had a bandwidth of only 8 GHz (most likely due to higher parasitics) we obtained a high RF output power of 10.2 dBm at 20 GHz and 5 V as shown in Fig. 7(b). The measurement was limited by the available optical input power as the device was not yet fully saturated. The IP3 was measured at 10 mA and 1 GHz and reached 34 dBm.

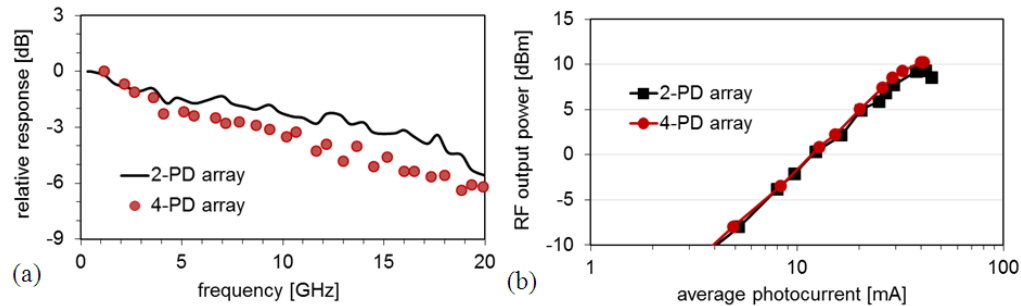


Fig. 7. (a) Frequency responses and (b) RF output power at 20 GHz and 5 V from 2- and 4-element PD arrays.

#### 4. Conclusion

Modified uni-traveling carrier photodiodes and arrays on SOI waveguides were fabricated and characterized. Single PDs reach up to 30 GHz bandwidth and deliver more than 2.5 dBm RF output power up to 40 GHz. Photodiode arrays exceed a saturation current-bandwidth-product of 630 mA·GHz and reach unsaturated RF output power levels of 12 dBm and 10 dBm RF at 8 GHz and 20 GHz, respectively. A measured IP3 of 30 dBm at 20 GHz and a low AM-PM conversion factor recommend the devices for high-linearity and high-power microwave photonic applications.

#### Acknowledgments

The authors thank Greg Fish, Anand Ramaswamy, and Jon Roth from Aurrion, Inc. for fruitful discussions. This work is supported by DARPA MTO under the DAHI program (E-PHI) contract HR0011-12-C-0006.